CCIT Report #551
August 2005

**For observing effects in the color images,
please view the electronic version of the paper on the computer monitor.**

Regularized Dehazing

Yoav Y. Schechner and Yuval Averbuch
Department of Electrical Engineering
Technion - Israel Institute of Technology.
Haifa 32000, Israel
yoav@ee.technion.ac.il , averbuch@tx.technion.ac.il

Abstract

When imaging in scattering media, the visibility degrades as objects become more distant. Visibility can be significantly restored by computer vision methods that account for physical processes occurring during image formation. Nevertheless, such recovery is prone to noise amplification in pixels corresponding to distant objects, where the medium transmittance is low. In this work we analyze the nature of this noise amplification. We then present an adaptive filtering approach that counters the above problems: while greatly improving visibility relative to raw images, it inhibits noise amplification. Essentially, the recovery formulation is regularized, where the regularization adapts to the spatially varying medium transmittance. Thus, this regularization does not blur close-by objects. We demonstrate the approach in experiments where the scene radiance and distance map are recovered in haze and underwater.

Keywords: Physics based vision, Color, Polarization, Vision in Bad Weather, Inverse problems, Dehazing, Defogging.

1 Introduction

Most current computer vision algorithms are designed for clear visibility conditions. However, images taken in turbid media such as fog, haze, and water suffer from poor-visibility. In such media, the radiance from a scene point is significantly altered due to scattering: it decays exponentially [26] with distance, and is compounded by stray light which increases with distance.

Automatic recovery of visual information in poor-visibility conditions would be beneficial to computer vision systems as well as human users. There is, thus, a growing interest in the analysis of such images [4, 8, 19, 26, 30]. Several methods have been proposed to restore good visibility. Some of them are based on acquiring multiple images of the same scene under different weather conditions [26]. Others use special active illumination hardware [9, 13, 18, 20, 28, 36, 44, 46, 47]. In some media, instant inversion of the image degradation can be performed based on analysis of two frames taken with different states of polarizing filter. This approach has proved effective in atmospheric haze [40]. Similarly, it has been applied underwater [38]. Visibility recovery can also be based on a single frame, if it is accompanied by a distance map of the scene.

Although significant progress has been achieved, prior studies into the subject have hardly dealt with noise. The object radiance decays exponentially with the object distance. Thus, noise is amplified when attempting to invert the degradation caused by the medium. Hence, noise in the restored images depends on distance. Far objects suffer from noise much more than close objects, since their attenuated signal is more strongly amplified in the inverse process. We wish to suppress the generated noise. Due to the physical nature of the noise amplification, the noise suppression should be adaptive to the distance map. This map may be based on light modulation [18, 20, 28, 44], auxiliary sensors [30], stereo vision [29] or be set interactively by a user [27, 43]. It may also be

estimated by analysis of frames taken through a polarizing filter [38, 40, 41].

This paper proposes an adaptive digital filtering approach, which is applicable to such scenarios. Our approach restores visibility while adaptively suppressing noise. We successfully applied this approach to images acquired in atmospheric haze and underwater. We obtained significant improvement of visibility and color over raw data, while restraining noise.

In the next sections, we first analyze the main causes for image degradation due to scattering, and the causes for noise amplification by inversion of this degradation. Then, we present an adaptive filtering approach that deals with these problems. We discuss numerical and analytical aspects, and present experimental results.

2 Theoretical Background

In this section, we mainly refer to visibility problems caused by atmospheric scattering. However, our analysis suits other scattering environments, particularly underwater. In this section we describe the image formation model. Then, we describe a naive inversion process of this model, in an attempt to recover clear visibility of the scene.

2.1 Visibility Degradation

Air is a scattering medium. Its scattering effect is greatly amplified by haze, consisting of small aerosols [26], or by fog, which is made of water droplets. As a ray of light progresses towards the viewer through this medium, part of its energy is scattered to other directions and a portion of it may be absorbed. When imaging, we sense two components. The first component originates from the radiance $L_{\text{object}}(x, y)$ of the scene object at distance $z(x, y)$ (see Fig. 1), where (x, y) are pixel coordinates. An attenuated and somewhat blurred

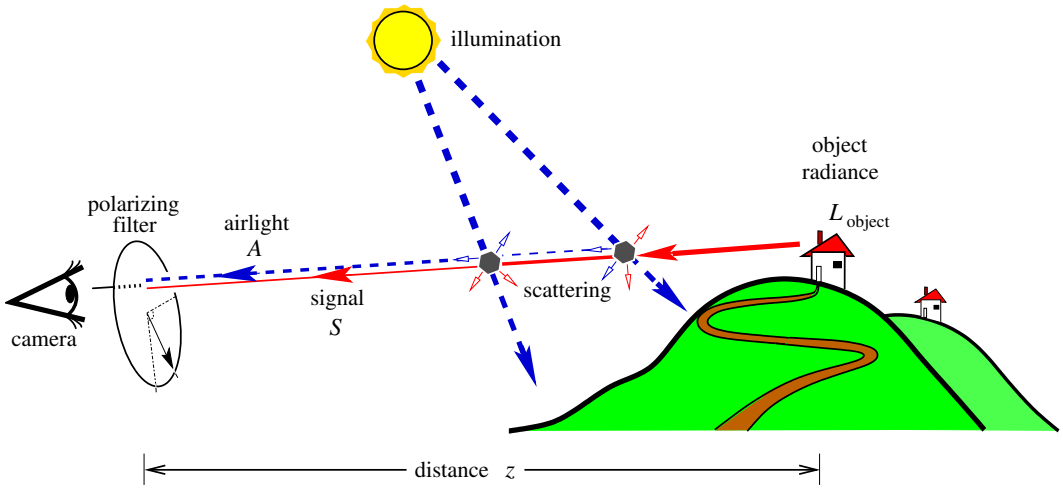

Figure 1: [Dashed rays] Light coming from the illuminant (e.g., Sun) and scattered toward the camera by atmospheric particles is the airlight A. The airlight increases with the distance z of the object. [Solid ray] The light emanating from the object is attenuated along the line of sight as z increases, leading to the signal S. Without scattering, the object radiance would have been L_{object}. The scene is imaged through a polarizing filter.

version of this radiance[1] is called here the *signal*. Motivated by studies which show that blur by scattering is *not* the dominating source of visibility degradation [14,39,40], we do not address this blur. Thus, the signal is given by

$$S(x, y) = L_{\text{object}} t(z) \ , \tag{1}$$

where

$$t(z) = \exp\left[-\int_0^z \beta(z')\, dz'\right] \tag{2}$$

is the medium transmittance. Here β is the extinction coefficient due to scattering and absorption. When the extinction coefficient is distance invariant, i.e., $\beta(z) = \beta$, then

$$t(z) = \exp(-\beta z) \ . \tag{3}$$

The other component originates from the ambient illumination. Part of the ambient light is scattered into the line of sight by the particles in the medium (see Fig. 1). In

[1]The scene radiance is measured by the detector plane of the camera. The detected image irradiance is proportional to the scene radiance. Since the proportionality depends on the optical system parameters and not on the medium, we treat the image irradiance and the scene radiance as equivalent.

the context of atmospheric imaging, this component is termed *airlight* [24, 41] or path radiance [10]. A similar phenomenon exists underwater, where it is referred to as veiling light [7,22,31,35,37,46,48], path radiance [14,24], spacelight [7,11,22,23,48], or backscatter [13, 24]. Assuming that the illumination over the line of sight is uniform [41], the airlight is

$$A(x,y) = A_\infty \left\{1 - t[z(x,y)]\right\} \ , \tag{4}$$

where A_∞ is the airlight radiance corresponding to an object at an infinite distance.

The overall measurement is the incoherent sum of the airlight and the signal

$$I = S + A \ . \tag{5}$$

It has been shown [10] that except for rather close objects, I is typically dominated by airlight. Thus, typically most of the light we measure is not attributed to the signal S, whose origin is L_{object}. This observation is partly due to the fact that most terrestrial objects have a low albedo [10], decreasing the signal.

In order to restore L_{object} we need to remove the additive airlight from the acquired observation. Then we need to compensate for the attenuation of the signal, that is caused by the scattering medium. As will be detail in Sec. 2.2, restoration may be formulated as a simple inversion of the image formation process (Eqs. 2-5). However, inverting the exponential attenuation (3) drastically amplifies even a negligible acquisition noise in pixels corresponding to distant objects. This problem is not specific to the atmosphere, but exists in all turbid media. As discussed in [39], the same noise amplification occurs in recovery of underwater scenes.

2.2 The Basic Inversion Method

In this section we briefly describe a simple method for visibility recovery. While being effective, this method is noise-sensitive. Suppose for the moment that we have an estimate

of the medium transmittance $t(x,y)$ and airlight $A(x,y)$ at each pixel. Based on Eqs. (1) and (5), recovery of the object radiance by a simple inversion process is

$$\widehat{L}_{\text{object}}(x,y) = \frac{I(x,y) - A(x,y)}{t(x,y)} \ . \tag{6}$$

Note that $I = I(x,y)$, $A = A(x,y)$ and $t = t(x,y)$. Hence, the inversion process (6) is formulated as being applied to each pixel independently. Therefore, the recovery is spatially adaptive, and implicitly adaptive to the distance $z(x,y)$.

There are two major ways to obtain $t(x,y)$ and $A(x,y)$, depending on whether we have prior knowledge of the distance map $z(x,y)$. We shall later comment on the possibility of having such knowledge. Meanwhile, suppose, as indeed we do for most of this paper, that we do not have such a prior map. To bypass this lack of knowledge we exploit the relationship between airlight and transmittance (4). Note that if we have an estimate of the airlight A, then by inverting Eq. (3), the estimated transmittance is

$$t(x,y) = \left[1 - \frac{A(x,y)}{A_\infty}\right] \ . \tag{7}$$

The airlight saturation value A_∞ is a global parameter which does not vary significantly across narrow fields of view. This parameter is estimated based on the image data (see [40, 41]), by measuring an image pixel that corresponds to an object at infinity (e.g., the sky close to the horizon).

In haze and water, we can estimate $A(x,y)$ by analyzing two frames acquired through a polarizer [38, 40, 41]. The frames correspond to two orientations of the polarizing[2] filter. The best results are achieved at orientations that lead to extrema (minimum and maximum) of the image irradiance. Denote these images by $I^{\max}(x,y)$ and $I^{\min}(x,y)$. The frame $I^{\min}(x,y)$ has the least amount of airlight, hence providing the best contrast a

[2]Analysis of a sequences of polarization filtered images has proved useful in various other computer vision problems [2, 3, 6, 25, 50].

raw image can deliver. Hence, we refer to it as the frame corresponding to the *best state* of the polarizer. Using both $I^{\max}(x,y)$ and $I^{\min}(x,y)$, the airlight is estimated by

$$A = \frac{I^{\max} - I^{\min}}{p} \ , \tag{8}$$

where $p \in [0,1]$ is the airlight degree of polarization. The parameter p is global. As described above for A_∞, it is estimated based on the raw frame values $I^{\max}$ and $I^{\min}$ (see [40, 41]), at an image pixel that corresponds to an object at infinity

$$p \equiv \frac{A_\infty^{\max} - A_\infty^{\min}}{A_\infty^{\max} + A_\infty^{\min}} \ . \tag{9}$$

Since Eq. (8) yields A, we can derive t using Eq. (7). We can then perform the inversion (6). This method assumes that the signal polarization is insignificant, and thus polarization is associated with the airlight. We note that I used in Eqs. (5,6) is given by

$$I = I^{\max} + I^{\min} \ , \tag{10}$$

thus

$$A_\infty = A_\infty^{\max} + A_\infty^{\min} \ \ . \tag{11}$$

If we had knowledge of the distance map of the scene by auxiliary sensors or by user interaction, recovery can be based on a single frame. Based on Eq. (3), $z(x,y)$ is transformed to $t(x,y)$, which then leads to the estimate of $A(x,y)$ by Eq. (4). This process would require knowledge of the global parameters β and A_∞, which do not vary much across the field of view. The latter can be extracted from the raw frame, as described above.

An example of an experimental implementation [40] of the method (6)-(11) is shown in Fig. 2. The recovered scene is much clearer than the raw data,[3] however, it is very

[3]For clarity of display, the luminance channel of the images shown in this paper have undergone the same standard contrast stretching, while their hue and saturation were untouched. This operation was done only towards the display. The algorithms described in the paper were run on raw, unstretched data.

Figure 2: [Top] An image of a hazy scene, corresponding to the best state of mounted polarizer. [Bottom] Dehazed image, using the basic algorithms of [40]. While contrast is significantly improved, noise is amplified in pixels corresponding to long distances.

noisy in pixels corresponding to distant objects. This is not surprising. As we already mentioned in Sec. 2.1, the transmittance t decreases exponentially with the distance z (see Eq. 3). Thus, the inversion (6) of this effect drastically amplifies noise.

3 Spatially Varying Noise

Noise and other disturbances are generated during the acquisition and the inversion processes. Before we propose an algorithm that suppresses noise, we first analyze the nature of noise amplification. This section focuses on noise in recovery that is based on polarization. Nevertheless, it gives a general indication that in images recovered from frames acquired in scattering media, the noise strongly depends on the spatially varying medium transmittance.

The noise variance is given by

$$\sigma^2_{L_{\text{object}}} = \left(\frac{\partial \widehat{L}_{\text{object}}}{\partial I^{\max}} \right)^2 \cdot \sigma^2_{I^{\max}} + \left(\frac{\partial \widehat{L}_{\text{object}}}{\partial I^{\min}} \right)^2 \cdot \sigma^2_{I^{\min}} \ , \tag{12}$$

where $\sigma_{I^{\max}}$ and $\sigma_{I^{\min}}$ denote noise variances in each of the raw images. From Eqs. (4), (8) and (6), it follows that

$$\frac{\partial \widehat{L}_{\text{object}}}{\partial I^{\max}} = \frac{1}{t^2} \left[\left(1 - \frac{1}{p} \right) t + \frac{L_{\text{object}} t}{p A_\infty} \right] \ , \tag{13}$$

$$\frac{\partial \widehat{L}_{\text{object}}}{\partial I^{\min}} = \frac{1}{t^2} \left[\left(1 + \frac{1}{p} \right) t - \frac{\widehat{L}_{\text{object}} t}{p A_\infty} \right] \ . \tag{14}$$

In the following we study different noise models.

3.1 Irradiance-Independent Noise

In this section we analyze noise that is independent of the image irradiance. Examples include quantization noise, read noise and dark current noise. Suppose that the overall noise can be expressed as an equivalent quantization noise. The quantization accuracy of the acquired images is 2^{-b}, where b is the number of *effective* bits the camera outputs per pixel. Therefore,

$$\sigma_{I^{\max}} = \sigma_{I^{\min}} = 2^{-b} \ . \tag{15}$$

By substituting Eqs. (13,14,15) in Eq. (12), the total noise variance is

$$\sigma^2_{L_{\text{object}}} = \frac{2^{1-2b}}{t^2}\left[1 + \frac{1}{p^2}\left(1 - \frac{L_{\text{object}}}{A_\infty}\right)^2\right] \ . \tag{16}$$

According to Eq. (16), the noise in the recovered image is partially dependent on the object radiance. More importantly, it is amplified as t decreases, i.e., at longer distances. Note that $1/t^2 \in [1, \infty)$. Thus, $1/t^2$ may amplify noise by up to an infinite factor. On the other hand, the range of L_{object} is practically finite, bounding its effect on (16). Hence, t has the crucial effect on noise amplification.

3.2 Shot Noise

In this section we analyze shot noise, which by nature depends on the acquired images. The variance of this noise is proportional to the image intensity

$$\sigma^2_{I^{\max}} = \kappa I^{\max} \ , \tag{17}$$

$$\sigma^2_{I^{\min}} = \kappa I^{\min} \ . \tag{18}$$

Here κ is a proportionality coefficient. It is inversely related to the number of detector generated electrons required for changing the camera readout by a single gray-level.

Using Eqs. (1,4,5,8,10,11),

$$I^{\max} = L_{\text{object}} t/2 + A^{\max}_\infty (1-t) \ , \tag{19}$$

$$I^{\min} = L_{\text{object}} t/2 + A^{\min}_\infty (1-t) \ . \tag{20}$$

Making further use of Eqs. (9,11),

$$I^{\max} = L_{\text{object}} t/2 + A_\infty (1+p)(1-t)/2 \ , \tag{21}$$

$$I^{\min} = L_{\text{object}} t/2 + A_\infty (1-p)(1-t)/2 \ . \tag{22}$$

Eqs. (21,22) determine the noise variances in Eqs. (17,18). When substituting these into Eq. (12), we obtain that the noise variance of the recovered image is simply

$$\sigma^2_{L_{\rm object}} = \kappa \frac{L_{\rm object}}{t} \quad . \tag{23}$$

Clearly, the noise $\sigma_{L_{\rm object}}$ strongly depends on t. Considering this result and the one derived in Sec. 3.1, we propose in this paper a noise suppression process by regularization, that is explicitly dependent on t.

3.3 Noise of Other Variables

It worth studying the noise of other variables involved in the estimation process, i.e., S, A and t. In the following, we show that these variables do not possess noise amplification that is spatially varying. For example, when estimating the airlight, the variance of the resulting noise is

$$\sigma^2_A = \left(\frac{\partial A}{\partial I^{\rm max}}\right)^2 \cdot \sigma^2_{I^{\rm max}} + \left(\frac{\partial A}{\partial I^{\rm min}}\right)^2 \cdot \sigma^2_{I^{\rm min}} \quad . \tag{24}$$

Using Eq. (8),

$$\sigma^2_A = \frac{\sigma^2_{I^{\rm max}} + \sigma^2_{I^{\rm min}}}{p^2} \quad . \tag{25}$$

Hence, the noise in the estimated airlight is similar to that of the raw frames, up to a global scale. It is not amplified in a spatially varying way. A similar analysis leads to the same conclusion regarding S and t. For this reason, if we want to filter noise in these variables, we do not need a special technique. We can use standard denoising, e.g., space invariant blur. Only when it comes to estimating $L_{\rm object}$, we encounter the need for adaptation.

4 Restoration with Adaptive Regularization

As was stated in previous sections, noise is amplified during recovery of pixels corresponding to distant objects. In Sec. 2.2, we showed a simple restoration algorithm. The

Figure 3: Standard noise filtering by a Gaussian kernel as applied to the dehazed image shown Fig. 2.

recovered image is much clearer, but noisy nevertheless. Applying standard smoothing may reduce noise at pixels corresponding to distant objects. The drawback of such an approach is degradation of resolution of nearby objects, since blur is induces by this digital processing. This blur is unjustified since only little noise exists in pixels corresponding to close by objects, as shown in Sec. 3. An example of noise suppression by a Gaussian smoothing filter may be seen in Fig. 3. Compare this image to Fig. 2. Indeed, we see degradation in resolution where it is not desired, i.e., at close objects. It becomes obvious that the desired noise suppression algorithm should adapt to the medium transmittance at each pixel.

We now gradually describe the proposed filtering approach. The proposed algorithm seeks the best fit to the inverse problem, while regularizing the estimate $\widehat{L}_{\text{object}}$:

$$\widehat{L}_{\text{object}} = \arg\min_{L_{\text{object}}} \varphi\left(L_{\text{object}}\right), \tag{26}$$

where φ is a cost function composed of a fitting term and a regularization term

$$\varphi\left(L_{\text{object}}\right) = \left(\text{Fitting} + \text{Regularization}\right) \ . \tag{27}$$

Let us first discuss the fitting term, which penalizes for deviation from the model described in Sec. 2. In principle, we could opt for a fitting term of the form

$$\text{Fitting}\,(L_{\text{object}},S,A,t) = \|S - tL_{\text{object}}\|^2 + \\ + \mu_S\|I-(S+A)\|^2 + \mu_t\|t - A/A_\infty\|^2 + \mu_A\|A-(I^{\max}-I^{\min})/p\|^2 \ , \quad (28)$$

where μ_S, μ_t and μ_A are constants. Apparently, Eq. (28) encapsulates all the model components: the signal attenuation relative to the sought L_{object}, the modelling of the measured intensity as a sum of the signal and airlight, the relation between the transmittance and the airlight, and finally, the polarization-based expression for airlight. However, such a formulation is inconvenient. It involves a large number of variables $(L_{\text{object}}, S, A, t)$ to be simultaneously optimized at each pixel. Moreover, it is unclear how the different parameters μ_S, μ_t and μ_A should be set.

Note, however, that the estimates of S, A and t do not exhibit spatially varying noise amplification (See Sec. 3.3). Hence, each of them can undergo standard space invariant filtering. We thus estimate A offline, and subsequently t. Based on Eq. (5), we then estimate the signal as

$$S(x,y) = I(x,y) - A(x,y) \ . \quad (29)$$

We do not regularize S, hence we maintain the details of the signal. Once we have an estimate of these variables, we remain with data fitting that explicitly involves the transmittance and the unknown L_{object}. Hence, the fitting term we use is

$$\text{Fitting} = \|S - \mathcal{T}L_{\text{object}}\|^2 \ , \quad (30)$$

where $\mathcal{T}$ ia a transmittance operator, which corresponds to the values of t across the image.

As for the regularization term, consider first the standard form

$$\text{Regularization} = \lambda\|\mathcal{D}L_{\text{object}}\|^2 \ , \quad (31)$$

where $\mathcal{D}$ is the Laplacian operator and λ is the weight of the regularization term. This term penalizes the cost function for unsmooth results. However, we wish to avoid any regularization in pixels corresponding to close pixels, for which $\mathcal{T} \to 1$. To aggressively impose adaptivity, we use a local weight in the regularization formulation that depends explicitly on t. Consider a regularization term of the form

$$\text{Regularization} = \lambda \left\| \mathcal{W}\mathcal{D}L_{\text{object}} \right\|^2 \ . \tag{32}$$

Here $\mathcal{W}$ is a weighting operator. It depends explicitly on the transmittance t at each pixel, hence implicitly adaptive to the object distance z. In the next sections we detail implementations of this approach in both monochrome and color images.

5 Adaptive Regularization in Monochrome Images

To perform the minimization, we may first convert all the images to column-stack vectors. The vector $\mathbf{s}$ denotes the signal, while $\mathbf{l}$ denotes the object radiance. We can then define the operators in terms of matrices. The cost function is thus

$$\varphi\left(\mathbf{l}\right) = \left\| \mathbf{s} - \mathbf{T}\mathbf{l} \right\|^2 + \lambda \left\| \mathbf{W}\mathcal{D}\mathbf{l} \right\|^2 \ , \tag{33}$$

where the attenuation operator is expressed by means of a diagonal matrix $\mathbf{T}$, whose diagonal elements express t at each corresponding pixel. The 2D Laplacian operator $\mathcal{D}$ is also expressed as a matrix operation over a vector, as described in [21]. The weighting matrix $\mathbf{W}$ is diagonal as well. We use a simple weighting matrix, whose elements are defined as

$$w_{ii} = \left(1 - t_{ii}\right)^2 \ \ , \tag{34}$$

where t_{ii} are the diagonal elements of $\mathbf{T}$. Note that $t_{ii} \in [0, 1]$. The proposed weighting emphasizes the regularization of pixels corresponding to distant objects (where $t_{ii} \to 0$), and turns off the regularization at close objects (where $t_{ii} \to 1$).

Eqs. (33) is minimized by standard linear optimization tools. Examples of restoration with this weighted regularization are shown in Fig. 4. It is important to note that the weighted regularization creates no blur at all in regions corresponding to close objects. There, the result is indistinguishable from that of simple inversion. On the other hand, the weighted regularization yields results that are less noisy than naive inversion at image regions corresponding to long distances. This noise reduction is traded for image blur in those regions. This trade off is controlled by the parameter λ. As we will see in Secs. 6 and 7, this blur is much less severe when the regularization approach is applied to color images.

6 Adaptive Regularization in Color Images

In this section we extend noise supression to color images. As we explain, it is better *not* to repeat the monochrome algorithm (Sec. 5) on each color channel separately. Rather, we make a modification to make it more plausible to human color perception.

6.1 RGB Formulation

A color image consists of three channels, representing the energy of red, green and blue wavelength bands, per pixel. At first sight it may appear that we need to apply the algorithm used in monochrome on each color channel separately. Such an approach combines a fitting term for each of the color channels and a corresponding regularization term. Define the column stack representation of object radiance in the red, green and blue color channels as $\mathbf{l}_{\mathrm{R}}$, $\mathbf{l}_{\mathrm{G}}$ and $\mathbf{l}_{\mathrm{B}}$, respectively. Let us encapsulate these vectors in a single column stack:

$$\mathbf{p} = \begin{bmatrix} \mathbf{l}_{\mathrm{R}} \\ \mathbf{l}_{\mathrm{G}} \\ \mathbf{l}_{\mathrm{B}} \end{bmatrix} \quad . \tag{35}$$

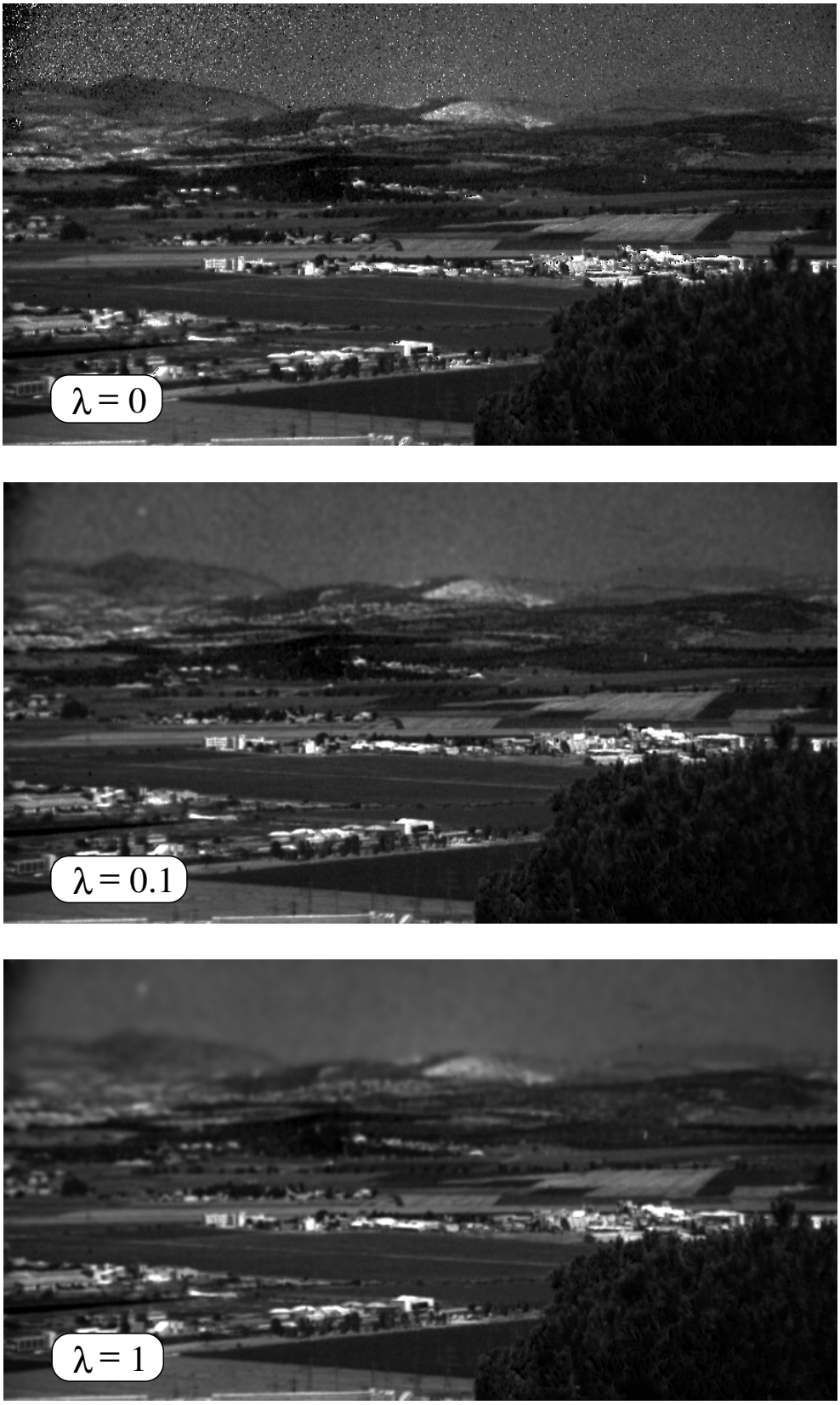

Figure 4: Monochrome restoration. As the weight λ of the regularization term increases, high frequency noise in the background is suppressed, while blurring the recovered image. These effects adapt to the object distance (transmittance).

The solution is now found as

$$\widehat{\mathbf{p}} = \arg\min_{\mathbf{p}} \varphi\left(\mathbf{p}\right) \quad , \tag{36}$$

where φ is the cost function, composed of fitting and regularization terms. We use

$$\text{Fitting} = \|\mathbf{s}_{\mathrm{R}} - \mathbf{T}_{\mathrm{R}}\widehat{\mathbf{l}}_{\mathrm{R}}\|^2 + \|\mathbf{s}_{\mathrm{G}} - \mathbf{T}_{\mathrm{G}}\widehat{\mathbf{l}}_{\mathrm{G}}\|^2 + \|\mathbf{s}_{\mathrm{B}} - \mathbf{T}_{\mathrm{B}}\widehat{\mathbf{l}}_{\mathrm{B}}\|^2 \quad , \tag{37}$$

where $\mathbf{s}_{\mathrm{R}}$, $\mathbf{s}_{\mathrm{G}}$ and $\mathbf{s}_{\mathrm{B}}$ are the signals at each color channel. The matrices $\mathbf{T}_{\mathrm{R}}$, $\mathbf{T}_{\mathrm{G}}$ and $\mathbf{T}_{\mathrm{B}}$ express the transmittance operator in each color channel.

Suppose the regularization is of the form

$$\text{Regularization} = \lambda_R\|\mathbf{W}\mathcal{D}\widehat{\mathbf{l}}_{\mathrm{R}}\|^2 + \lambda_G\|\mathbf{W}\mathcal{D}\widehat{\mathbf{l}}_{\mathrm{G}}\|^2 + \lambda_B\|\mathbf{W}\mathcal{D}\widehat{\mathbf{l}}_{\mathrm{B}}\|^2 \, , \tag{38}$$

where λ_R, λ_G and λ_B are the weights of the components in this term. This term regularizes each color channel independently. Experiments show that using the formulation (37) and (38) sometimes results in color distortion, when the recovered image is visualized. We hypothesize that this may happen because human color perception does not comply with spatial processing of separate wavelength bands, rather than a combinations of color channels. Moreover, such a formulation does not take advantage of perceptual properties of spatial resolution to reduce the apparent blur. In the next section we describe how we account for these issues.

6.2 Perceptually Motivated Formulation

As detailed in Sec. 6.1, perceptual considerations may not favor separate spatial processing of color channels. We thus transfer the images to a better representation. Note that human vision is less sensitive to blur of chromatic information than to luminance blur. We can exploit this to suppress noise while making the consequent blur less apparent. We achieve this by switching from the RGB color space to the NTSC YIQ color space,[4] when treating the regularization term.

[4]The NTSC YUV color space may be used as well.

The RGB to NTSC conversion is given by

$$\begin{bmatrix} \mathbf{l}_{\mathtt{Y}} \\ \mathbf{l}_{\mathtt{I}} \\ \mathbf{l}_{\mathtt{Q}} \end{bmatrix} = \begin{bmatrix} \alpha_{\mathrm{Y}} & \beta_{\mathtt{Y}} & \gamma_{\mathtt{Y}} \\ \alpha_{\mathrm{I}} & \beta_{\mathtt{I}} & \gamma_{\mathtt{I}} \\ \alpha_{\mathrm{Q}} & \beta_{\mathtt{Q}} & \gamma_{\mathtt{Q}} \end{bmatrix} \begin{bmatrix} \mathbf{l}_{\mathtt{R}} \\ \mathbf{l}_{\mathtt{G}} \\ \mathbf{l}_{\mathtt{B}} \end{bmatrix} \quad , \tag{39}$$

where $\mathbf{l}_{\mathtt{Y}}$, $\mathbf{l}_{\mathtt{I}}$ and $\mathbf{l}_{\mathtt{Q}}$ are the values of each of the components in the YIQ space. Details of the elements of the matrix used in Eq. (39) are given in [12]. This representation expresses the luminance in the `Y` component, separately from the chromatic components `I` and `Q`. We preferred to use this linear transformation, rather than nonlinear color spaces as Hue-Saturation-Value. The reason is that a linear transformation fits naturally into the linear optimization we perform, as we detail in Sec. 6.3.

It is important to note that we apply this transformation *only* in the regularization term. We do not apply it to the fitting term. The reason is that fitting is derived from the original inverse problem (6), which is wavelength dependent through all its parameters: the image irradiance I, the airlight A and the transmittance t. The relationship between these variables is physical, rather than perceptual, and is wavelength dependent. Had we used the YIQ color space in the fitting term, we would have lost the physical relevance of the wavelength dependance. Hence, the fitting term is maintained in the RGB color space.

While we maintain the fitting term as in (37), we use the following regularization term:

$$\text{Regularization} = \lambda_{\mathtt{Y}} \|\mathbf{W}\mathcal{D}\mathbf{l}_{\mathtt{Y}}\|^2 + \lambda_{\mathtt{C}} \|\mathbf{W}\mathcal{D}\mathbf{l}_{\mathtt{I}}\|^2 + \lambda_{\mathtt{C}} \|\mathbf{W}\mathcal{D}\mathbf{l}_{\mathtt{Q}}\|^2 \quad , \tag{40}$$

where $\lambda_{\mathtt{Y}}$ is the weight of the luminance regularization and $\lambda_{\mathtt{C}}$ is the weight of the chrominance regularization. We use $\lambda_{\mathtt{C}} > \lambda_{\mathtt{Y}}$: selecting a relatively large $\lambda_{\mathtt{C}}$ suppresses noise in image components for which human vision tolerates blur, while keeping a small $\lambda_{\mathtt{Y}}$ minimizes blur in the component that is perceptually dominant.

In Eq. (40) we used the same weighting matrix $\mathbf{W}$ as defined in Eq. (34). To determine the weights, we used the transmittance of a single color channel. In haze, we used the

transmittance of the green color channel to determine the regularization weights, while in water we used the blue channel. We opted for these channels since they typically contain the highest light energies in the respective media, hence presumably yielding better distance maps for use in the weighting.

6.3 Gradient and Hessian

To minimize the cost function (36), we apply standard optimization tools. Such optimization benefits from knowledge of the gradient and the Hessian of φ. In this section we derive these functions. Define a vector that encapsulates vectors $\mathbf{s}_{\mathrm{R}}$, $\mathbf{s}_{\mathrm{G}}$ and $\mathbf{s}_{\mathrm{B}}$ in a single column stack,

$$\mathbf{s}_{\mathrm{RGB}} = \begin{bmatrix} \mathbf{s}_{\mathrm{R}} \\ \mathbf{s}_{\mathrm{G}} \\ \mathbf{s}_{\mathrm{B}} \end{bmatrix} , \tag{41}$$

and a matrix

$$\mathbf{T}_{\mathrm{RGB}} = \begin{bmatrix} \mathbf{T}_{\mathrm{R}} & \dots & 0 \\ \vdots & \mathbf{T}_{\mathrm{G}} & \vdots \\ 0 & \dots & \mathbf{T}_{\mathrm{B}} \end{bmatrix} . \tag{42}$$

The cost function defined by Eqs. (37) and (40) is

$$\varphi(\mathbf{p}) = \|\mathbf{s}_{\mathrm{RGB}} - \mathbf{T}_{\mathrm{RGB}}\mathbf{p}\|^2 + \lambda_{\mathtt{Y}}\|\mathbf{W}\mathcal{D}\Phi_{\mathtt{Y}}\mathbf{p}\|^2 + \lambda_{\mathtt{C}}\|\mathbf{W}\mathcal{D}\Phi_{\mathtt{I}}\mathbf{p}\|^2 + \lambda_{\mathtt{C}}\|\mathbf{W}\mathcal{D}\Phi_{\mathtt{Q}}\mathbf{p}\|^2 , \tag{43}$$

where the matrices $\Phi_{\mathtt{Y}}$, $\Phi_{\mathtt{I}}$ and $\Phi_{\mathtt{Q}}$ are defined as

$$\Phi_{\mathtt{Y}} = \begin{bmatrix} \alpha_{\mathtt{Y}}\mathbf{I} & \beta_{\mathtt{Y}}\mathbf{I} & \gamma_{\mathtt{Y}}\mathbf{I} \end{bmatrix} , \tag{44}$$

$$\Phi_{\mathtt{I}} = \begin{bmatrix} \alpha_{\mathtt{I}}\mathbf{I} & \beta_{\mathtt{I}}\mathbf{I} & \gamma_{\mathtt{I}}\mathbf{I} \end{bmatrix} , \tag{45}$$

$$\Phi_{\mathtt{Y}} = \begin{bmatrix} \alpha_{\mathtt{Q}}\mathbf{I} & \beta_{\mathtt{Q}}\mathbf{I} & \gamma_{\mathtt{Q}}\mathbf{I} \end{bmatrix} , \tag{46}$$

while $\mathbf{I}$ is the identity matrix. The α, β and γ coefficients used in Eqs. (44-46) are the ones used in Eq. (39), as defined in [12].

The gradient and Hessian of the fitting term are given by

$$\mathbf{g}_{\mathrm{Fitting}} = 2\mathbf{T}_{\mathrm{RGB}}^T \left[\mathbf{T}_{\mathrm{RGB}}\mathbf{p} - \mathbf{s}_{\mathrm{RGB}}\right] \tag{47}$$

and

$$\mathbf{H}_{\text{Fitting}} = 2\mathbf{T}_{\text{RGB}}^{T}\mathbf{T}_{\text{RGB}} \ , \tag{48}$$

respectively, where T denotes transposition. The gradient and Hessian of the regularization term are given by

$$\mathbf{g}_{\text{Regularization}} = 2\lambda_{\mathtt{Y}}\Phi_{\mathtt{Y}}^{T}\mathcal{D}\mathbf{W}^{T}\mathbf{W}\mathcal{D}\Phi_{\mathtt{Y}}\mathbf{p} + \\ + 2\lambda_{\mathtt{C}}\Phi_{\mathtt{I}}^{T}\mathcal{D}\mathbf{W}^{T}\mathbf{W}\mathcal{D}\Phi_{\mathtt{I}}\mathbf{p} + 2\lambda_{\mathtt{C}}\Phi_{\mathtt{Q}}^{T}\mathcal{D}\mathbf{W}^{T}\mathbf{W}\mathcal{D}\Phi_{\mathtt{Q}}\mathbf{p} \tag{49}$$

and

$$\mathbf{H}_{\text{Regularization}} = 2\lambda_{\mathtt{Y}}\Phi_{\mathtt{Y}}^{T}\mathcal{D}\mathbf{W}^{T}\mathbf{W}\mathcal{D}\Phi_{\mathtt{Y}} + \\ + 2\lambda_{\mathtt{C}}\Phi_{\mathtt{I}}^{T}\mathcal{D}\mathbf{W}^{T}\mathbf{W}\mathcal{D}\Phi_{\mathtt{I}} + 2\lambda_{\mathtt{C}}\Phi_{\mathtt{Q}}^{T}\mathcal{D}\mathbf{W}^{T}\mathbf{W}\mathcal{D}\Phi_{\mathtt{Q}} \ , \tag{50}$$

respectively. Hence, the gradient of the cost function is

$$\mathbf{g}_{\varphi(\mathbf{p})} = \mathbf{g}_{\text{Fitting}} + \mathbf{g}_{\text{Regularization}} \tag{51}$$

while the Hessian is

$$\mathbf{H}_{\varphi(\mathbf{p})} = \mathbf{H}_{\text{Fitting}} + \mathbf{H}_{\text{Regularization}} \ . \tag{52}$$

It is clear that the hybrid use of RGB in the fitting term and YIQ in the regularization term poses no mathematical complication in the optimization. The cost function, its gradient and its Hessian are derived in close form . This simplicity stems from the linear relation (39) between these color spaces.

7 Experimental Results

This section shows result of our method in several experiments. Despite variations of instruments and media, all the experiments use the *same* cost-function parameters. The luminance and chromatic regularization weights are $\lambda_{\mathtt{Y}} = 1/20$ and $\lambda_{\mathtt{C}} = 1/2$, respectively.

Figure 5: The image corresponding to Figs. 2 and 3 recovered with adaptive filtering.

7.1 In Haze

An example of restoration with our weighted regularization is shown in Fig. 5. Compare this color image to the naive inversion result and the raw image in Fig. 2. While visibility has improved significantly relative to the raw image, weighted regularization yields results that are less noisy than those of naive inversion. Note that close objects are not blurred at all.

An additional set of experimental results is shown in Fig. 6. As in the previous example, two images were taken through a polarizing filter. Here the images were acquired using a Nikon D-100 digital camera, where the mode of data extraction maintained a linear radiometric response. The transmittance map t recovered by this method is depicted in Fig. 7. It is equivalent to the distance map of the scene. To better observe the adaptive attenuation of noise, a strip of the scene is magnified in Fig. 8.

Figure 6: An additional experiment of dehazing by adaptive filtering. [Top] The raw image at the best state of the polarizer. [Bottom] Result of the algorithm.

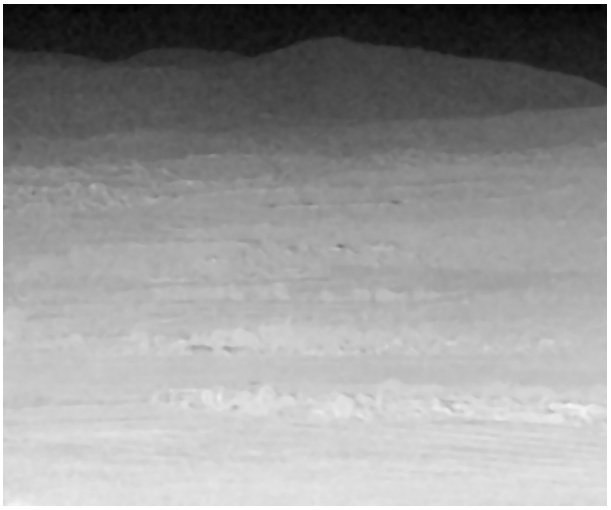

Figure 7: The recovered transmittance in the experiment corresponding to Fig. 6. It is equivalent to the distance map.

7.2 Underwater

We ran our method on an underwater scene, which had been imaged via a polarizer [39] by a Nikon D-100 in a housing. The raw frames were taken in natural illumination, and are shown in Fig. 9. They were acquired in the sea, 26 meters under the water surface. They are very blue, due to the strong attenuation of the red illumination component in these depths. The frames are displayed contrast stretched (as all images in this paper), and hence look very similar to one another. To partly compensate for the color imbalance, we attempted to normalize the image color by the color of a nearby sand-patch [39]. The left part of Fig. 10 shows the result of this operation, based on the raw image at the best state of the polarizer. This result still suffers from poor visibility.

We then applied our algorithm. Fig. 11 shows the transmittance map t (equivalent to the distance map) recovered by the method. We used it in the transmittance-adaptive optimization. We applied white balancing to the result of the optimization. The recovered image is shown on the right part of Fig. 10. The visibility has improved significantly, particularly for distant objects.

Figure 8: Zooming in on a region of the scene from Fig. 6. Dehazing by simple inversion achieves great visibility and color improvement, yet with high frequency noise in the background. Dehazing by adaptive filtering attenuates this noise, while sparing consequent blur from foreground objects.

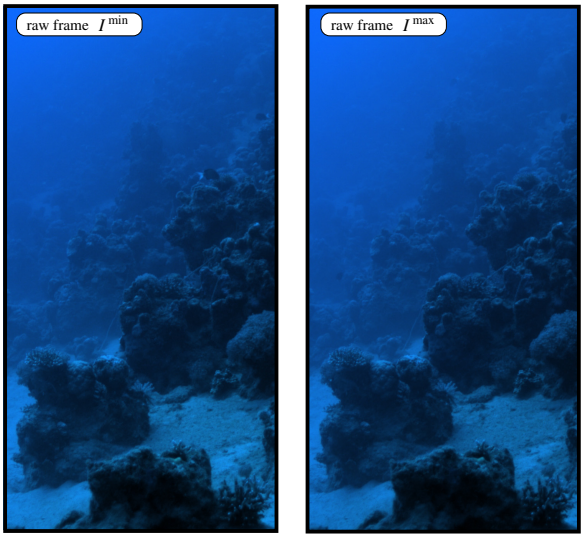

Figure 9: Raw color images (contrast stretched for display) of an underwater scene taken in the sea.

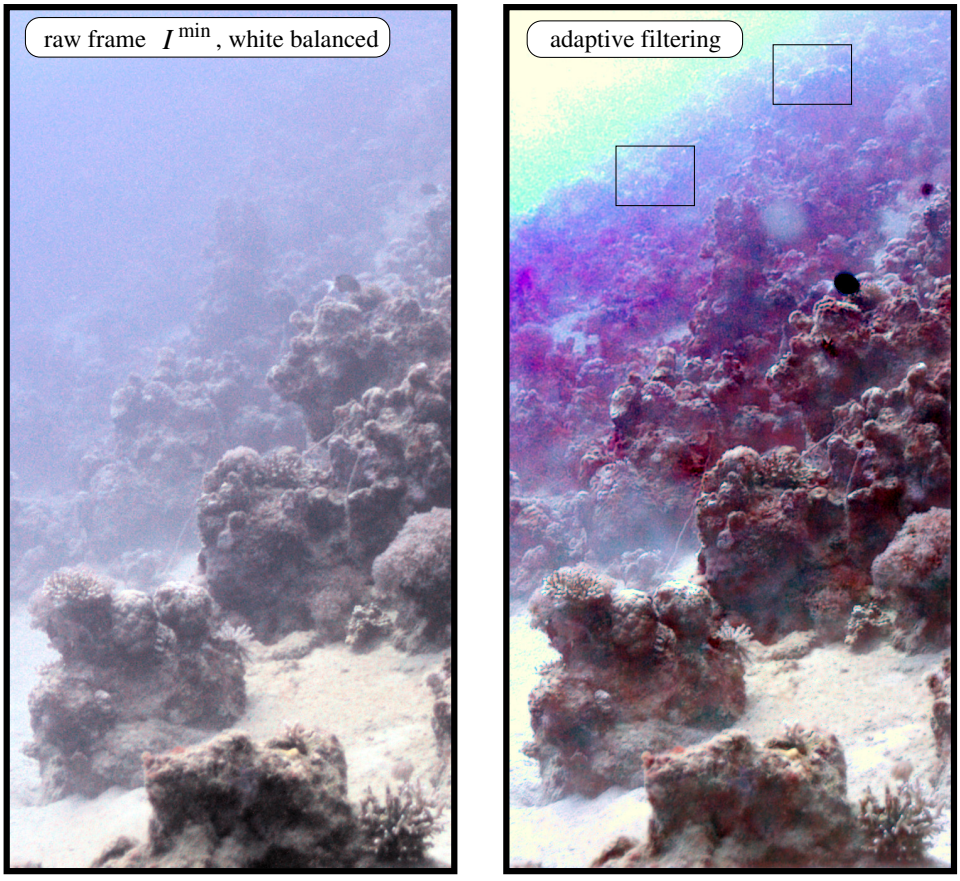

Figure 10: Processing of the images shown in Fig. 9. [Left] Simple white balancing of the raw frame does not reveal distant details. [Right] The result of applying adaptive filtering to remove path radiance, attenuation and noise, prior to white balancing. Details of distant objects are much better seen. The marked rectangular areas on the right are magnified in Fig. 12.

Figure 11: The recovered transmittance in the experiment corresponding to Fig. 9. It is equivalent to the distance map.

It is interesting to compare the results of adaptive regularization to those of simple inversion. Fig. 12 shows these results in two rectangular areas cropped from Fig. 10. A close look at this figure reveals that regularization *increased* a little the contrast and clarity. In the example on the right part of Fig. 12, features are more salient in the adaptively filtered (denoised) version, shown on the bottom, than their state in the noisy image shown on top. The same applies to the example on the left part of Fig. 12. Hence in this experiment, regularization does not appear to have caused loss of perceived quality due to blur, but the contrary. In the following we propose a possible explanation to this effect.

The explanation may stem from the depth of field of the raw frames. Underwater, depth of field is typically much narrower than in open air, for two reasons. First, the relevant distances in water are very close: meters, even centimeters, while in hazy air the distances relevant to this method are four orders of magnitude larger. Hence, in the open

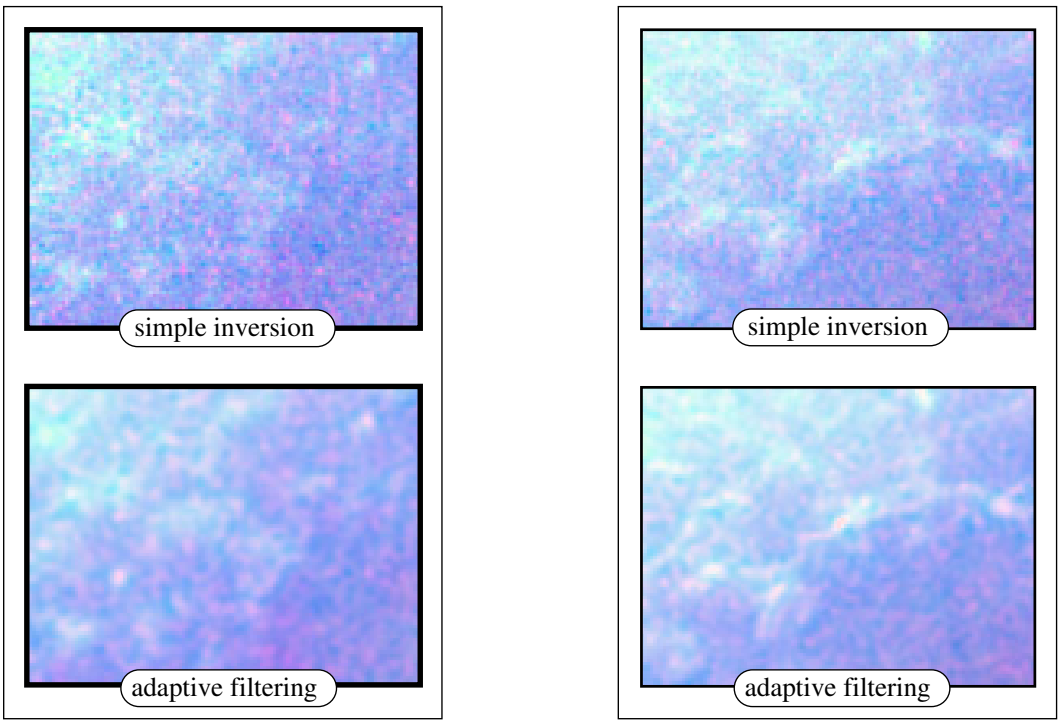

Figure 12: Magnification of the rectangular areas marked in Fig. 10. For each area, compare the result of standard inversion to that of adaptive filtering. **To observe the color effects, please view the paper on the computer monitor.**

air most of the distant scene corresponds to a "focus at infinity" state, while in water much of the scene in defocused (except for a narrow range). Second, the underwater darkness imposes use of the full lens aperture (narrowing the depth of field), while in the open air the aperture can often be narrow. Hence, in Fig. 9, the distant areas are *defocus blurred*, when the focus is set on closer objects. Thus, the energy of the signal corresponding to distant objects is limited to low spatial frequencies. For this reason, the recovered image $\widehat{L}_{\text{object}}$ is *not degraded* there by the digital smoothing that stems from regularization. While the signal is unaffected, regularization suppresses the high intensity, high frequency noise there. Hence the net result is some improvement of image clarity.

8 Discussion

We showed in this paper an adaptive filtering approach which is simple, yet effective. It significantly enhances color and contrast of scenes taken in scattering media, while countering noise amplification in a spatially varying adaptive way. The method capitalizes on human perception characteristics to achieve the goal with reduced consequent digital blur. Moreover, it appears that this digital blur does not degrade the recovered image in very turbid media, while still blurring out the noise. The reason is that high turbidity imposes low lighting (requiring high lens aperture) and short imaging distances, thus involving defocusing effects in the raw frames. The proposed approach exploits standard tools for efficient optimization.

We demonstrated the approach in haze and underwater, under natural illumination. Nevertheless, we believe that it applies to other media (such as tissue) and imaging systems, such as those based on active illumination [9,13,18,20,28,36,44,46,47]. In active illumination, the radiation is attenuated by the medium for approximately twice the object distance, beyond the $1/z^2$ falloff of the illumination incident on the object, caused by free space propagation. Hence, the signal there is also strongly distance dependent. Recovery in these circumstances may thus benefit from such distance-adaptive regularization to restrain noise amplification in the recovery.

The approach may be helpful in domains that are unrelated to scattering media. Spatially varying transmittance is not limited only to such media, but also to the imaging system itself. Most imaging systems have spatial non-uniformity due to vignetting and foreshortening [1,15,16,21,42,49,51]. This non-uniformity of optical transmittance tends to darken the periphery of frames. Compensating for this effect by digital post-processing increases image noise. Moreover, this noise amplification may disrupt image registration [42]. In such cases, the algorithm developed here can be directly employed by using

the spatially varying transmittance of the camera rather than the medium transmittance.

We would like to note that an important extension of this work is to use other weighting operators than the one we used. In particular, avoidance of edge smoothing can be attempted. A possible way to achieve it is to use a weighting operator

$$\widetilde{\mathcal{W}} = \frac{1}{\sqrt{1 + \xi |\nabla L_{\text{object}}|^2}} \mathcal{W} \quad , \tag{53}$$

where ∇L_{object} is the gradient of the dehazed scene and $\xi > 0$ is a control parameter. Here $\mathcal{W}$ is adaptive to the transmittance (distance), as defined in this paper, while the other term in $\widetilde{\mathcal{W}}$ ensures that regularization is weakened across edges, where ∇L_{object} is large. Edge preserving filtering has indeed been implemented with established numerical schemes, known as anisotropic diffusion [33] or Beltrami flow [17]. Other implementations use bilateral filtering [5, 45], automatic image partition [32] or line fields [34]. Thus, it would be interesting to merge these techniques with our distance-adaptive weighting.

Acknowledgments

Yoav Schechner is a Landau Fellow - supported by the Taub Foundation, and an Alon Fellow. The work was supported by the Israeli Science Foundation (grant no. 315/04), and the Magneton program of the Israeli Ministry of Commerce. The work was done in collaboration with ElOp Ltd. We wish to thank Einav Namer for her help in image acquisition and Michael Elad for useful discussions and optimization advice. The work was conducted in the Ollendorff Minerva Center in the Elect. Eng. Dept. at the Technion. Minerva is funded through the BMBF.

References

[1] M. Aggarwal and N. Ahuja. A pupil-centric model of image formation. *Int. J. Computer Vision*, 48:195–214, 2002.

[2] M. Ben-Ezra. Segmentation with invisible keying signal. *Proc. IEEE Conf. Computer Vision and Pattern Recognition*, Vol. 1, pp. 32-37, 2000.

[3] O. G. Cula, K. J. Dana, D. K. Pai and D. Wang. Polarization multiplexing for bidirectional imaging. *Proc. IEEE Conf. Computer Vision and Pattern Recognition*, Vol. 2 pp. 1116-1123, 2005.

[4] F. Cozman and E. Kroktov. Depth from scattering. *Proc. IEEE Conf. Computer Vision and Pattern Recognition*, pp. 801-806, 1997.

[5] F. Durand and J. Dorsey. Fast bilateral filtering for the display of high-dynamic-range images. *ACM Trans. on Graphics*, 21(3):257–266, 2002.

[6] H. Farid and E. H. Adelson. Separating reflections and lighting using independent components analysis. *Proc. IEEE Conf. Computer Vision and Pattern Recognition*, Vol. 1, pp. 262-267, 1999.

[7] E. Gaten, P. M. J. Shelton and M. S. Nowel. Contrast enhancement through structural variations in the rhabdoms of oplophorid shrimps. *Marine Biology*, 145:499–504, 2004.

[8] L. Grewe and R. R. Brooks, Atmospheric attenuation reduction through multi-sensor fusion. *Proc. SPIE*, vol. 3376, pp. 102-109, 1998.

[9] S. Harsdorf, R. Reuter and S. Tönebön, Contrast-enhanced optical imaging of submersible targets. *Proc. SPIE*, vol. 3821, pp. 378–383, 1999.

[10] R. C. Henry, S. Mahadev, S. Urquijo and D. Chitwood. Color perception through atmospheric haze. *Journal of the Optical Society of America A*, 17:831–835, 2000.

[11] G. Horváth and D. Varjú. *Polarized Light in Animal Vision*, chapter 14,25,26,28. Berlin: Springer, 2004.

[12] K. Jack. *Video Demystified*, chapter 3, page 17. LLH Technology Publishing, Eagle Rock, VA 2001.

[13] J. S. Jaffe. Computer modelling and the design of optimal underwater imaging systems. *IEEE J. of Oceanic Engineering*, 15:101–111, 1990.

[14] W. S. Jagger and W. R. A. Muntz. Aquatic vision and the modulation transfer properties of unlighted and diffusely lighted natural waters. *Vision Research*, 33:1755–1763, 1993.

[15] J. Jia and C. K. Tang. Image registration with global and local luminance alignment. *Proc. IEEE Computer Vision and Pattern Recognition*, Vol. I, pp. 156-163, 2003.

[16] S. B. Kang and R. Weiss. Can we calibrate a camera using an image of a flat, textureless lambertian surface? *Proc. European Conf. Computer Vision*, Part. 2, pp. 640-653, 2000.

[17] R. Kimmel. *Numerical Geometry of Images: Theory, Algorithms, and Applications*. Berlin: Springer, 2003.

[18] D. M. Kocak and F. M. Caimi. Computer vision in ocean engineering. in *The Ocean Eng. Handbook*, F. El-Hawari, Ed., ch. 4.3 CRC Press, 2001.

[19] N. S. Kopeika. *A System Engineering Approach to Imaging*, pp. 446-452. Bellingham, Wash: SPIE, 1998.

[20] M. Levoy, B. Chen, V. Vaish, M. Horowitz, I. McDowall and M. Bolas, Synthetic aperture confocal imaging. *Proc. SIGGRAPH*, 2004.

[21] A. Litvinov and Y. Y. Schechner. Radiometric framework for image mosaicking. *Journal of the Optical Society of America A*, 22:839-848, 2005.

[22] J. N. Lythgoe. The adaptation of visual pigments to the photic environment. In *Handbook of Sensory Physiology*, volume VII/1, chapter 14, 566–603. Berlin: Springer-Verlag, 1972.

[23] J. N. Lythgoe and C. C. Hemmings. Polarized light and underwater vision. *Nature*, 213:893–894, 1967.

[24] B. L. McGlamery. A computer model for underwater camera system. *Proc. SPIE*, volume 208, pages 221–231, 1979.

[25] D. Miyazaki and K. Ikeuchi. Inverse polarization raytracing: estimating surface shape of transparent objects. *Proc. IEEE Conf. Computer Vision and Pattern Recognition*, Vol. 2, pp. 910-917, 2005.

[26] S. G. Narasimhan and S. K. Nayar. Vision and the atmosphere. *International Journal of Computer Vision*, 48:233–254, 2002.

[27] S. G. Narasimhan and S. K. Nayar. Interactive deweathering of an image using physical models. *Proc. IEEE Workshop on Color and Photometric Methods in Computer Vision,*, 2003.

[28] S. G. Narasimhan, S. K. Nayar, B. Sun and S. J. Koppal. Structured Light in scattering media. *Proc. IEEE International Conference on Computer Vision,* To be published, 2005.

[29] S. Negahdaripour and H. Madjidi. Stereovision imaging on submersible platforms for 3D mapping of Benthic habitats and sea floor structures. *IEEE J. Oceanic Eng.,* 28:625-650 2003.

[30] J. P. Oakley and B. L. Satherley, Improving image quality in poor visibility conditions using a physical model for contrast degradation. *IEEE Trans. on Image Processing* 7:167-179, 1998.

[31] L. Peichl, G. Behrmann and R. H. H. Kröger. For whales and seals the ocean is not blue: a visual pigment loss in marine mammals. *European J. of Neuroscience*, 13:1520–1529, 2001.

[32] J. Polzehl and V. G. Spokoiny. Adaptive weights smooting with applications to image restoration. *J. of Royal Stat. Soc., Ser. B*, 62:335-354, 2000.

[33] P. Perona and J. Malik. Scale-space and edge detection using anisotropic diffusion. In *IEEE Trans. Pattern Analysis and Machine Intelligence*, 12:629–639, 1990.

[34] A. N. Rajagopalan, S. Chaudhuri and U. Mudenagudi. Depth estimation and image restoration using defocused stereo pairs. *IEEE Trans. Pattern Pattern Analysis and Machine Intelligence*, 26:1521-1525, 2004.

[35] G. G. Rosenthal and M. J. Ryan. Visual and acoustic communication in non-human animals: A comparison. *Journal of Biosciences*, 25:285–290, 2000.

[36] M. P. Rowe, E. N. Pugh Jr., J. S. Tyo and N. Engheta, Polarization-difference imaging: a biologically inspired technique for observation through scattering media. *Optics Lett.*, 20:608–610, 1995.

[37] N. Shashar, R. Hagan, J. G. Boal and R.T. Hanlon. Cuttlefish use polarization sensitivity in predation on silvery fish. *Vision Research*, 40:71–75, 2000.

[38] Y. Y. Schechner and N. Karpel. Clear underwater vision. *Proc. IEEE Computer Society Conference on Computer Vision and Pattern Recognition*, volume 1, pages I–536–543, 2004.

[39] Y.Y. Schechner and N. Karpel. Recovering scenes by polarization analysis. *Proc. MTS/IEEE Oceans* , volume 3, pages 1255–1261, 2004.

[40] Y. Y. Schechner, S. G. Narasimhan and S. K. Nayar. Polarization-based vision through haze. *Applied Optics*, 42:511–525, 2003.

[41] Y. Y. Schechner, S. G. Narasimhan and S. K. Nayar. Instant dehazing of images using polarization. *Proc. IEEE Computer Society Conference on Computer Vision and Pattern Recognition*, volume 1, pages I–325–332, 2001.

[42] Y. Y. Schechner and S. K. Nayar Generalized Mosaicing: High Dynamic Range in a Wide Field of View. *International Journal of Computer Vision*, 53:245–267 , 2003.

[43] J. Sun, J. Jia, C. K. Tang H. Y. Shum Poisson matting. *ACM Transactions on Graphics*, 23:315–321, 2004.

[44] B. A. Swartz. Laser range gate underwater imaging advances. *Proc. MTS/IEEE OCEANS*, pp. 722–727, 1994.

[45] C. Tomasi and R. Manduchi. Bilateral filtering for gray and color images. *Proc. IEEE Int. Conf. Computer Vision*, pp. 839-846, 1998.

[46] J. S. Tyo, M. P. Rowe, E. N. Pugh Jr. and N. Engheta. Target detection in optically scattering media by polarization-difference imaging. *App. Opt.*, 35:1855–1870, 1996.

[47] J. G. Walker, P. C. Y. Chang and K. I. Hopcraft. Visibility depth improvement in active polarization imaging in scattering media. *App. Opt.*, 39:4933–4941, 2000.

[48] R. Wehner. Polarization vision - a uniform sensory capacity? *J. Experimental Biology*, 204:2589–2596, 2001.

[49] R. G. Wilson and S. A. Shafer. What is the center of the image? *J. Opt. Soc. America A*, 11:2946-2955, 1994.

[50] L. B. Wolff. Polarization-based material classification from specular reflection. *IEEE Trans. Pattern Analysis and Machine Intell.*, 12:1059-1071, 1999.

[51] W. Yu. Practical anti-vignetting methods for digital cameras. *IEEE Trans. on Cons. Elect.*, 50:975-983, 2004.